Structural Engineering and Mechanics, Vol. 40, No. 5 (2011) 617-636
DOI: http://dx.doi.org/10.12989/sem.2011.40.5.617

High-velocity impact of large caliber tungsten projectiles on ordinary Portland and calcium aluminate cement based HPSFRC and SIFCON slabs. Part II: numerical simulation and validation

P. Gülkan[1] and H. Korucu*[2]

[1]Department of Civil Engineering, Cankaya University, 06810 Ankara, Turkey
[2]Turkish Naval Forces Command, 06100 Bakanlıklar, Ankara, Turkey

(Received March 3, 2011, Revised Octover 6, 2011, Accepted October 21, 2011)

Abstract. We present the numerical implementation, simulation, and validation of the high-velocity impact experiments that have been described in the companion article. In this part, numerical investigations and simulations performed to mimic the tests are presented. The experiments were analyzed by the explicit integration-based software ABAQUS for improved simulations. Targets were modeled with a damaged plasticity model for concrete. Computational results of residual velocity and crater dimensions yielded acceptable results.

Keywords: high-velocity impact; projectile; calcium aluminate cement; steel fibers; simulation; SIFCON; ABAQUS explicit

1. Introduction

In the companion to this article (Korucu and Gülkan 2011), high velocity impact experiments on high-performance steel fiber reinforced concrete targets with and without reinforcement was described. The tungsten projectiles had a muzzle velocity over 4 Mach. Production and experimentation processes of four groups of specimens were described. The first group specimens were produced using ordinary CEM I 42.5 R cement based reinforced concrete. The second and third group of specimens contained 2 percent by volume of steel fibers with CEM I 42.5 R and Calcium Aluminate Cement (CAC40) based reinforced concrete, respectively. In the fourth group, SIFCON specimens including 12 percent of steel fibers by volume without reinforcement were tested. A high-speed camera was used to capture impact and residual velocities.

Prediction of the tests was simulated using ABAQUS/Explicit (Dassault Systemes 2007). It is intended here to present the results of numerical computations to simulate and validate the field experiments. The principal index will be the entry and exit velocities of the projectile striking the targets because we measured those variables in the field. Visual similarity of cratering and volume of ejected concrete are also used as measures of goodness of computations. The principal aim of this

*Corresponding author, Ph.D., E-mail: korucu_h@yahoo.com

article is to confirm that the extreme damage caused by a supersonic-velocity projectile penetrating a concrete target can be predicted with reasonable accuracy.

The ammunition we have used to target the concrete specimens is intended for armored targets. This type of ordnance is very expensive and rarely used outside of military applications because it is fired by a tank. Our objective was to investigate the accuracy of tools of computational mechanics in such an exercise, so our simulations are not misplaced.

Much of the body of knowledge derived from research and development pertaining to conventional weapons effects on hardened structures is strictly classified. With supersonic-velocity projectile firing weapons this restriction appears to be more acute because of the security concerns that revelation of test results or analysis procedures may carry. We were not encumbered by such restrictions because our research objective was limited to verifying the accuracy of computational procedures for only one type of weapon used against regular targets manufactured from commonly available concretes.

Hong *et al.* (2008) performed simulations of two/multiple shots impacting on a metallic component where the impact velocity of steel shots was 75 m/s to validate another experimental study. They used the same computational tool as we did, ABAQUS/Explicit. Shiu *et al.* (2008) carried out a Discrete Element Method based analysis in the companion to an experimental study of 34.5 kg flat-nose missile impacting on reinforced concrete targets with a velocity of 151 m/s. Rousseau *et al.* (2008) compared the performance of Finite Element and Coupled Finite Element/Discrete Element approach in the impact analysis of 40 m/s projectiles on concrete structures. Kumar (2010) carried out impact analysis on laminated composite cylindrical shells. A procedure for the reliability assessment of underground concrete barriers against the impact of a missile with a mass of 182 kg and a velocity of 411 m/s (1.2 Mach) was presented by Siddiqui *et al.* (2009). Huang *et al*. (2005) reported simulations performed by LS-DYNA where the impact of steel projectiles impacting on reinforced concrete targets with a striking velocity of 743 m/s (or 2.2 Mach). None of these studies has considered the effects of the sort of weapon that is reported in this article that provided a 4.2-Mach strike velocity. This represents the velocity range where empirical equations used in some applications for bullet penetration or scabbing effects are inapplicable.

2. Numerical analysis and simulations

Numerical simulations were performed by ABAQUS/Explicit Version 6.7-1 (Dassault Systemes 2007) a software package with several concrete models. The principal aim of these simulations was to validate the experimental results and observe the effect of dense reinforcement, steel fibers and concrete type in crater formation and velocity reduction.

As pointed out in the Part I of the study (Korucu and Gülkan 2011), some shots were missed by the high-speed cameras due to poor weather conditions or asynchronous recording. These shots are excluded here.

Simulations of the shots that involved more than one specimen were executed individually, i.e., when multiple specimens were subjected to successive impact, several individual analyses were performed in succession with impact velocities equal to exit velocities from the intervening targets.

The notation is given in Appendix A.

2.1 Numerical simulations

To achieve improved predictive power, numerical simulations that allow the engineer to define a parameter-defined material model must be used. Computer codes as ABAQUS/Explicit (Dassault Systemes 2007) can provide information on stress and deformation fields under conditions resembling the field test conditions. This code was chosen to back-calculate the behavior of the specimens. ABAQUS/Explicit provides the capability to introduce constitutive and failure modes of materials. This is its most important advantage over empirical formulations.

The plastic-damage model in ABAQUS is described in Appendix B. It is based on the models proposed by Lubliner *et al.* (1989) and by Lee and Fenves (1998). The damaged plasticity concrete model is primarily intended to provide a general capability for the analysis of concrete structures under cyclic and/or dynamic loading. The model is also suitable for the analysis of other quasi-brittle materials, such as rock, mortar and ceramics.

2.2 Numerical model: preliminaries

Three dimensional finite element models of reinforced concrete specimens and the projectile were developed. One-quarter of the physical model was used in the analyses. Taking advantage of the two-way symmetry reduced the duration of analyses. The outer edges of the quarter model were assumed to be fixed against translation. To mesh the concrete specimen and reinforcing bars hexahedral elements were used. The projectile, except for its nose part, was also defined by hexahedral elements. The nose was defined as tetrahedral due to its more complex shape. Mesh size varied between 10 mm and 14 mm. The model consisted approximately of 450 000 elements. Time step, Dt, was at an order of 10^{-9} s because the very high velocity of the projectile as it bore through the mesh caused very high strain rates that needed to be captured.

The calculations were very time-consuming, so a single analysis lasted nearly a week on a PC of 1.67 GHz Core 2 Duo processors and 2 GB memory. We did not include the transverse (along thickness) reinforcement in our model in the interest of keeping a properly regular mesh. Modeling

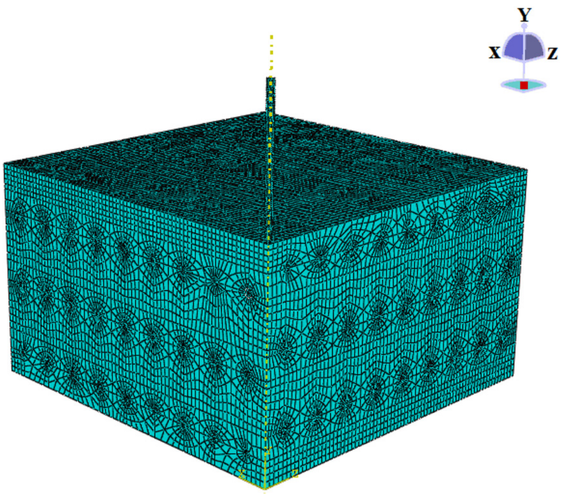

Fig. 1 One-quarter FE model

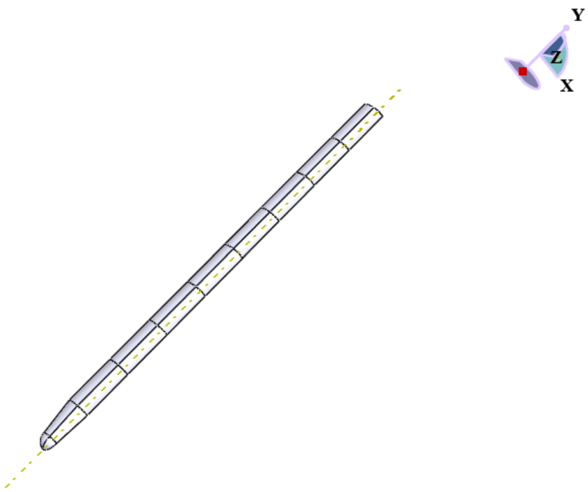

Fig. 2 One-quarter FE model of projectile

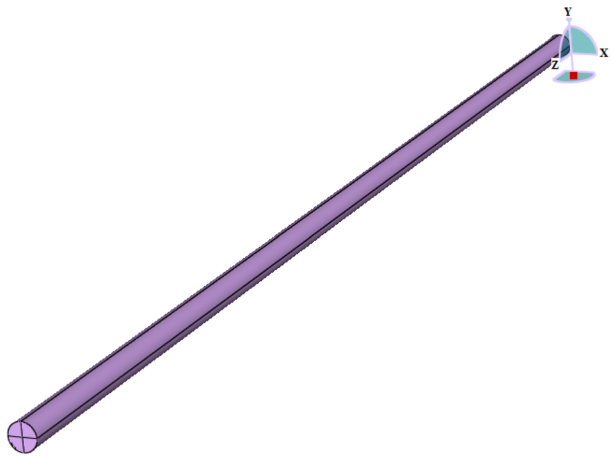

Fig. 3 Geometric model of the reinforcing bars

reinforcement exactly as it was in actual design sometimes led to irregular meshing. Finite element modeling of reinforced concrete specimen and the projectile is illustrated in Figs. 1-2.

2.3 Material modeling

In the calculations, concrete was assumed to be homogeneous. A supersonic projectile impacting a concrete target produces extremely high strain rates for the part of the material in the vicinity of its path and very high temperatures in the same confined region. This could be ascertained during our post-impact inspections. No attempt was made to couple these effects into the concrete model because of the lack of basic data. Even when highly sophisticated models are used in computational programs it appears that the accurate description of the constitutive behavior of the materials remains as a major challenge. Traditional material test results are the first level properties that can describe the nominal material properties. The background test data consisted of traditional stress-strain curves for the types of concrete that was used in fabricating the specimens, obtained under typical laboratory conditions. We rationalized that this was likely to be the extent of the input data available under most circumstances, so we used the idealized, strain-rate and temperature-independent stress-strain curves in both compression and tension for the three groups for which projectile entry and exit velocities had been measured. Stress-strain curves for compressive and flexural behavior of concrete obtained from sample tests, adjusted and idealized as appropriate, were used. Tensile behavior of concrete containing 2 percent of steel fibers used in the second group of specimens was described for the code from Bhargava *et al.* (2006) and Li (2001). Tensile stress-strain curve for SIFCON containing 12 percent of steel fibers were obtained from Naaman (1992). The complete array of constitutive relations for specimen Groups 1, 2 and 4 are shown in Fig. 4. In each case, frames on the left are the idealized compressive constitutive curves and those on the right are for tension.

Concrete slabs were modeled using “Damaged Plasticity Model” for concrete. A “Rate-Independent Plasticity Model” for steel was used in modeling the bars. The theory and modeling parameters for the computational exercise are described in Appendix B for concrete and in Appendix C for steel.

Other parameters such as initial elastic modulus and Poisson’s ratio for concrete were rounded

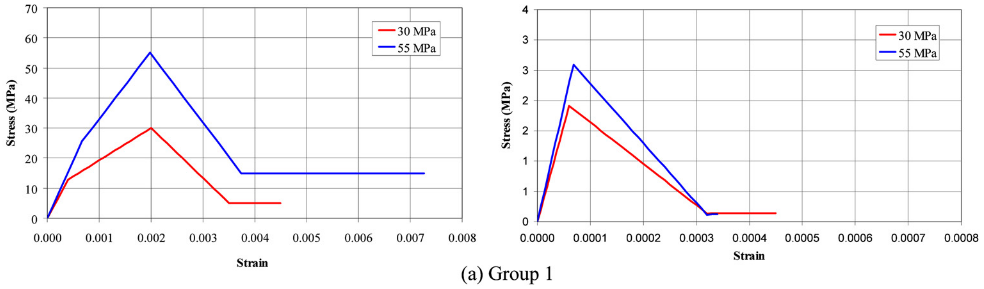

(a) Group 1

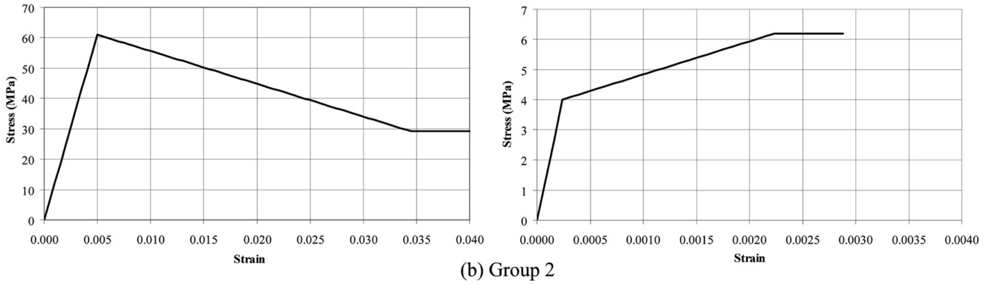

(b) Group 2

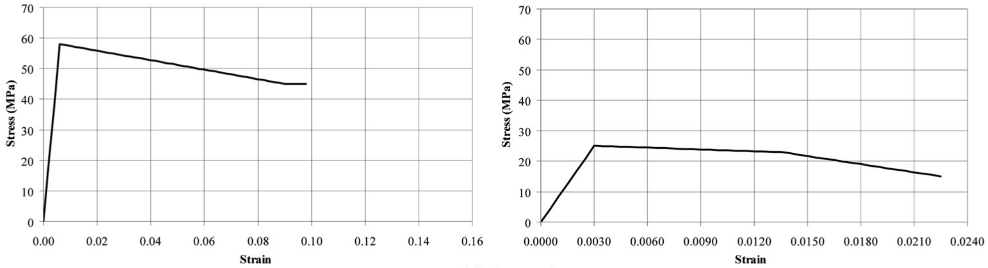

(c) Group 4

Fig. 4 Idealized stress-strain curves for the specimens analyzed

Table 1 Material parameters used for concrete in the calculations

	Group 1			Group 2			Group 4		
	1-2	1-3	1-4	2-1	2-2	2-3	4-1	4-2	4-3
σ_c^c, MPa	30	30	55	61	61	61	58	58	58
σ_t^c, MPa	1.92	1.92	2.60	6.20	6.20	6.20	25	25	25
E, GPa	38	38	40	12	12	12	10	10	10
υ_c		0.2			0.2			0.2	

uniformly for all cases as from laboratory tests (Table 1). These values for steel were $E = 237.5$ GPa and $\upsilon = 0.3$ (see Table 2).

The material of the projectile was tungsten. The main objective of the study was to investigate the behavior of reinforced concrete under impact, so the projectile was assumed as "non-eroding". Elastic modulus and Poisson's ratio for tungsten were defined as $E = 11$ GPa and $\upsilon = 0.3$, respectively (Table 3).

Table 2 Material parameters used for steel in the calculations

Bar diameter	Φ 10 mm	Φ 18 mm	Φ 22 mm
σ_y^s, MPa	600.5	480.4	477.2
σ_u^s, MPa	702.3	608.3	664.9
E_s, GPa	237.5	237.5	237.5
ν_s	0.3	0.3	0.3

Table 3 Material parameters used for tungsten in the calculations

E_t, GPa	ν_t
411	0.3

2.4 Impact modeling

The computational projectile struck each slab with the initial velocity obtained from high-speed camera recordings. The contact between the projectile and the slab was defined by "all with self" option under "general contact" selection in ABAQUS/Explicit. This option enabled inclusion of frictional effects in the calculations. Each strike was analyzed individually. The principal reason for this choice of modeling was the run-time of the simulation. Individual runs allowed intervening to fix run-time errors. When the deformation in any element reached 80 percent of the limiting strains in Fig. 4 either in compression or in tension that element was assumed to have failed, and was no longer included in the remainder of the computational stream.

3. Results and discussions of simulations

In this part crater sizes and entry-exit velocities obtained from experimental studies and simulations are compared. These were the only quantities that could be measured during and following the strike by the projectile but it is essential that they should be related to the empirical evidence. Simulation results are shown visually in Figs. 5-13 in a manner that allows comparison with the actual photograph of a given specimen, and calculated results are listed in Tables 4-6. Because of space limitations a 3D view of simulation is illustrated in Fig. 5 only for Specimen 1-2 of Group 1, which is shown with less detail in Fig. 6.

It should be noted that in the experiments, parts of concrete specimens subjected to projectile impact directly were wholly deformed, but because of intensive emplacement of longitudinal reinforcement and transverse confinement, these appear as if they have been perforated only in the same size as the projectile itself. In contrast, the volume of concrete between the craters at the front and rear sides of specimens must be assumed as having physically failed. Concrete mesh elements that reached 80 percent of their deformation capacity were deleted but for reinforcement no such deletion was made. Bars abutting the symmetry axis in all of Figs. 5-13 show clearly the magnitude of the large strains that they have undergone. Severe concrete disintegration occurs as a result.

Specimens 1-1, 2-1, 3-1 and 4-1 were targeted individually while specimens 1-2/1-3/1-4, 2-2/2-3, 3-2/3-3 and 4-2/4-3 were arrayed at 2 m spacing between each other and targeted collectively. The bullets entering Specimens 1-1, 2-1, 3-1 and 3-2/3-3 could not be captured by the high-speed

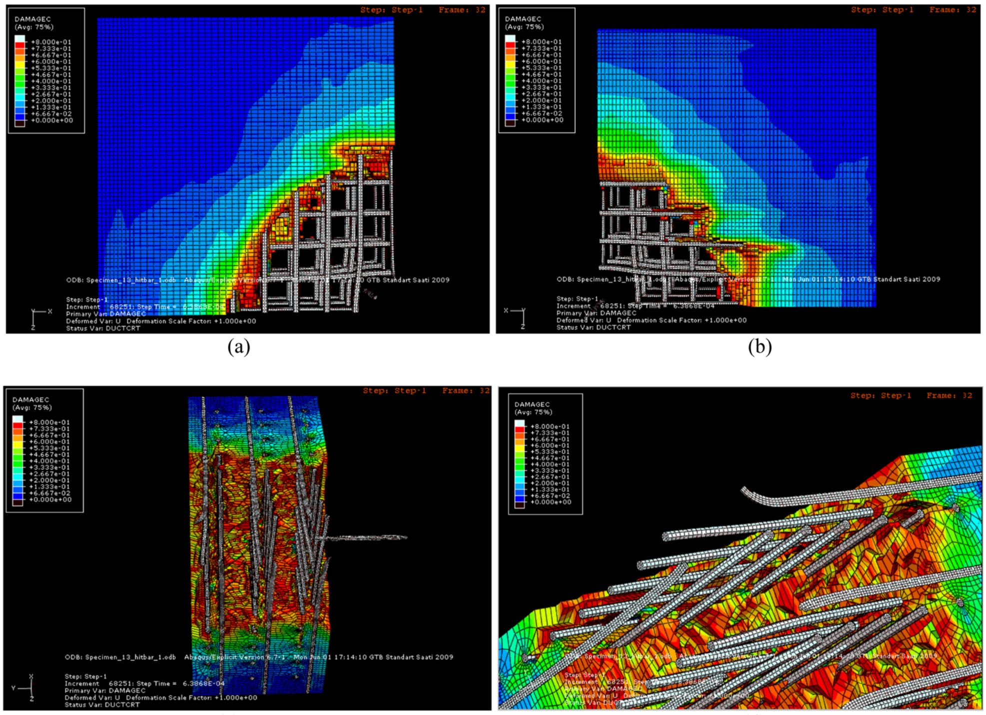

(a) (b) (c) (d)

Fig. 5 Deformed shape of specimen 1-2 in 3D-views (a) Front, (b) Rear, (c) Cross-section, (d) Close-up

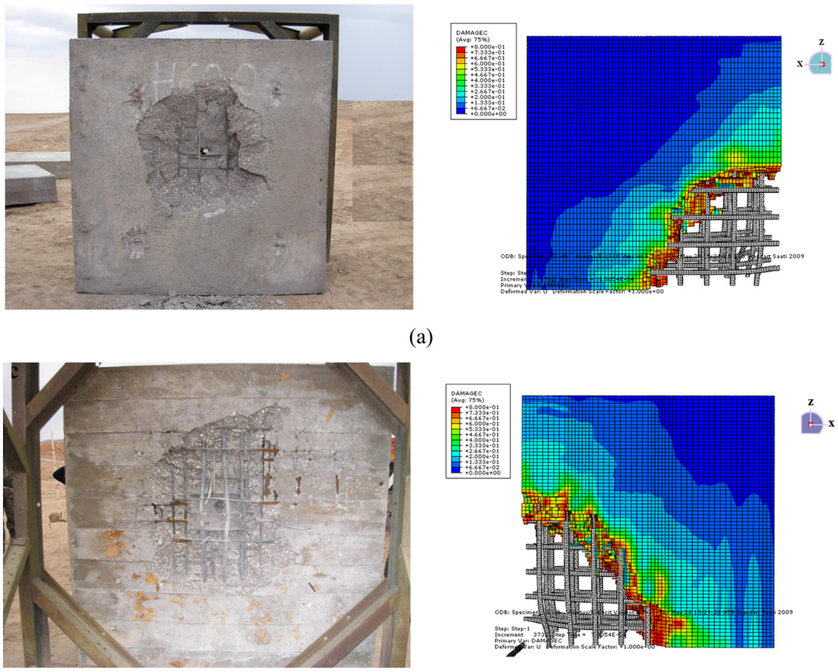

(a) (b)

Fig. 6 Comparison of the deformation of specimen 1-2 (a) Front, (b) Rear

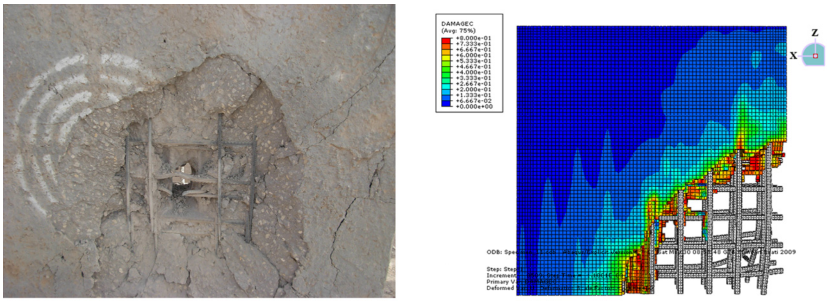

(a)

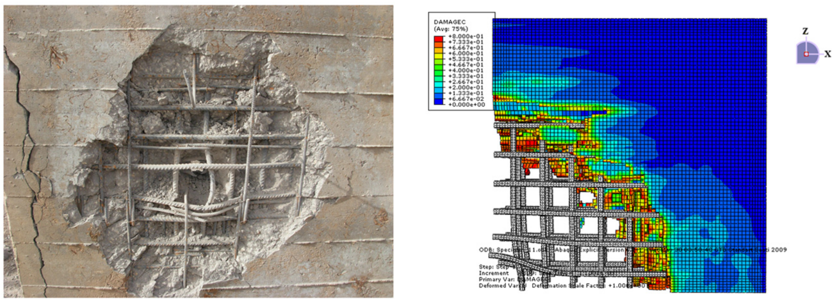

(b)

Fig. 7 Deformed shape of specimen 1-3 (a) Front, (b) Rear

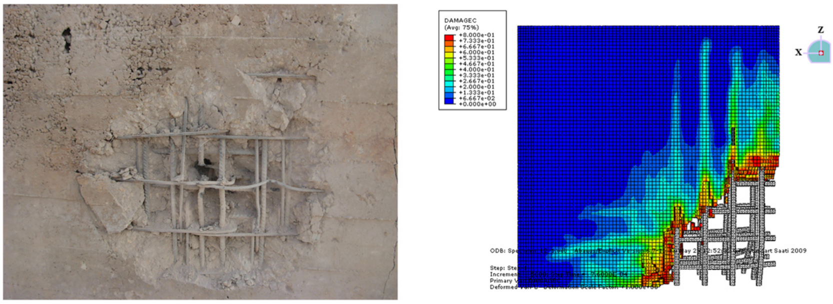

(a)

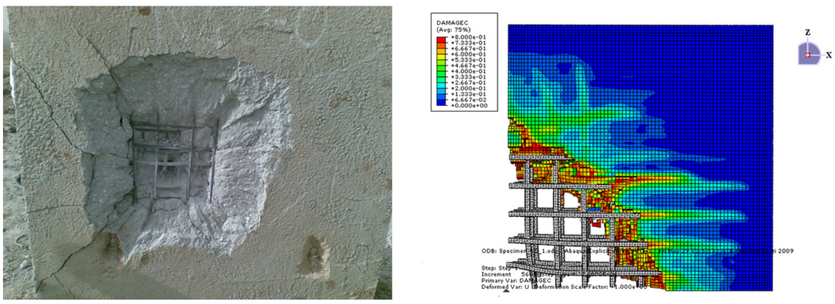

(b)

Fig. 8 Deformed shape of specimen 1-4 (a) Front, (b) Rear

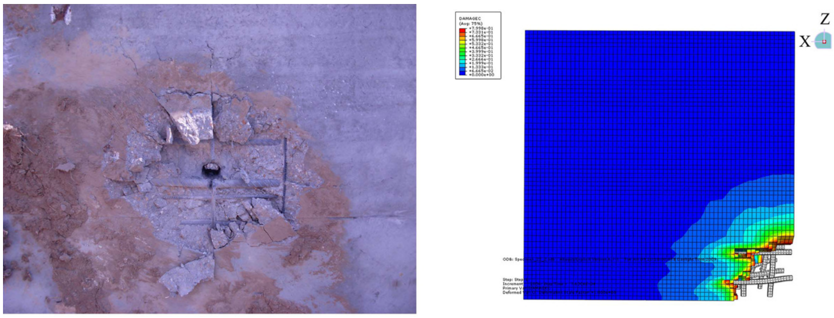

(a)

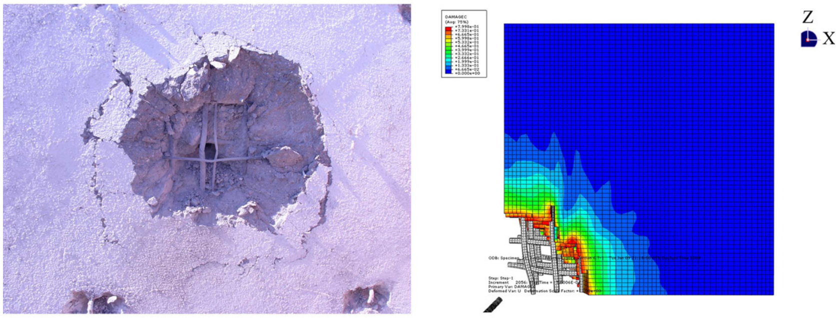

(b)

Fig. 9 Deformed shape of specimen 2-2 (a) Front, (b) Rear

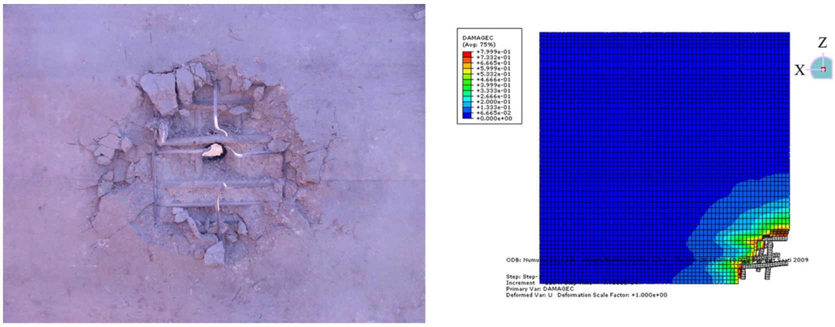

(a)

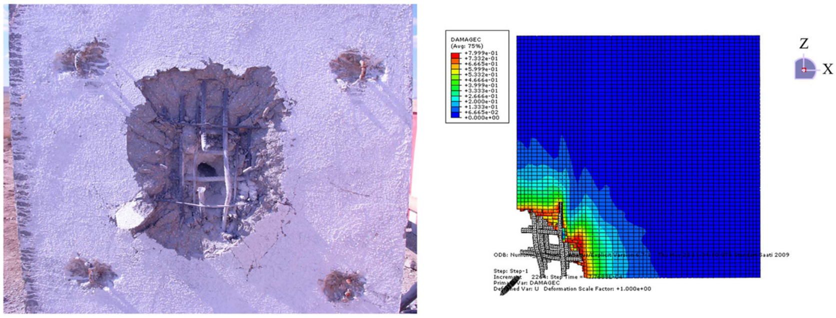

(b)

Fig. 10 Deformed shape of specimen 2-3 (a) Front, (b) Rear

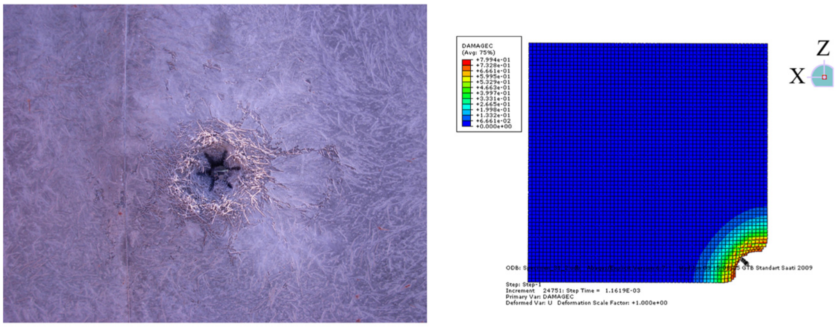

(a)

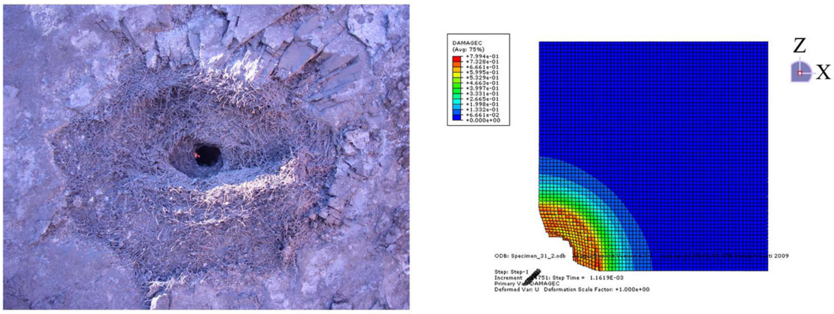

(b)

Fig. 11 Deformed shape of specimen 4-1 (a) Front, (b) Rear

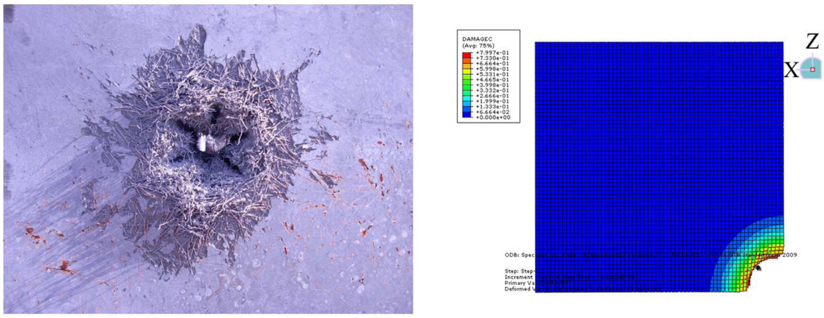

(a)

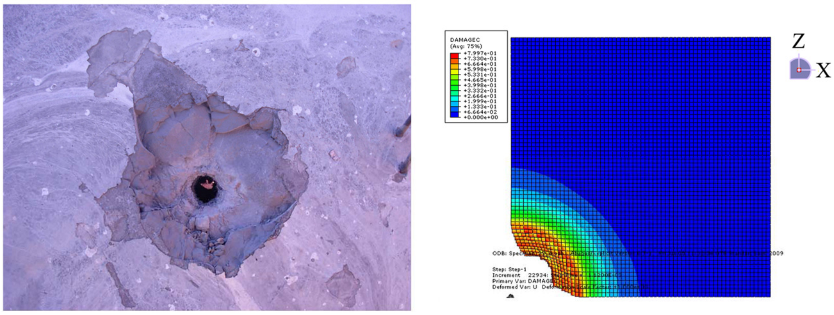

(b)

Fig. 12 Deformed shape of specimen 4-2 (a) Front, (b) Rear

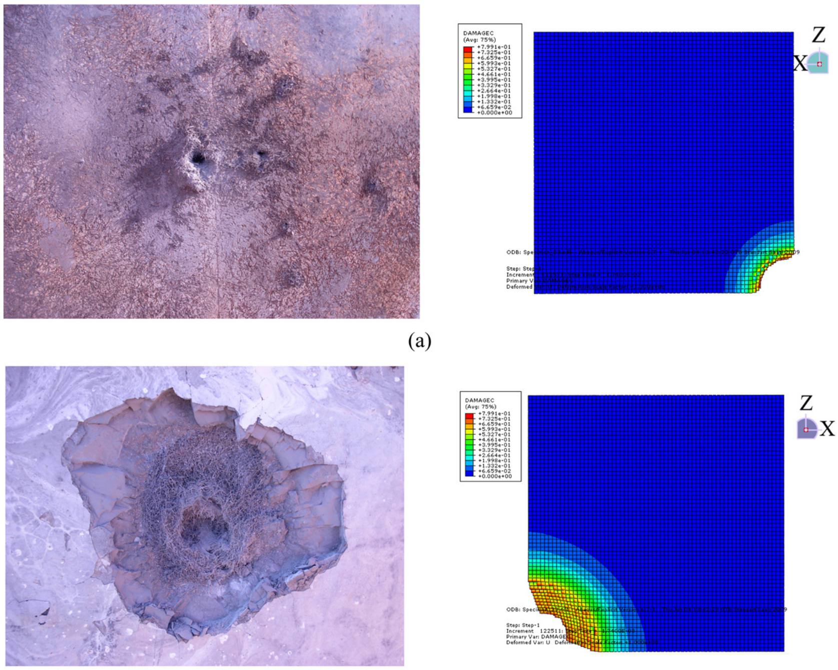

(a)

(b)

Fig. 13 deformed shape of specimen 4-3 (a) Front, (b) Rear

Table 4 Comparison of front face crater dimensions

Front face diameter (mm)						
	Experimental		Computational		Error (%)	
Specimen No.	Horiz.	Vert.	Horiz.	Vert.	Horiz.	Vert.
1-2	630	690	1050	940	66.6	36.2
1-3	840	900	1040	950	23.8	5.5
1-4	910	790	1020	1040	12.1	31.6
2-2	530	440	510	480	3.8	9.1
2-3	640	650	410	450	35.9	30.8
4-1	150	160	300	280	100	75
4-2	150	170	340	260	126.6	52.9
4-3	160	220	320	270	100	22.7

cameras because of asynchronous signaling between the gunner and the cameraman so they have not been included in the following narrative.

In any computational simulation of physical tests, incorporation of material properties into the calculation tool is the most important requirement to obtain well-matched results with the experiments. To do so, all relevant material tests must be performed during the production of specimens that will serve as the input for the computations. In this study, only compressive and flexural strength of concrete and tensile strength of steel bars were measured while other characteristics were imported

Table 5 Comparison of rear face crater dimensions

	Rear face diameter (mm)					
	Experimental		Computational		Error(%)	
Specimen No.	Horiz.	Vert.	Horiz.	Vert.	Horiz.	Vert.
1-2	860	840	1170	970	36.1	15.4
1-3	1080	950	1130	1080	4.6	13.6
1-4	1040	980	1190	1040	4.4	6.1
2-2	810	670	580	640	28.4	4.5
2-3	750	940	470	530	37.3	43.6
4-1	490	540	450	530	8.1	1.8
4-2	460	480	540	520	17.3	8.3
4-3	720	650	550	520	23.6	20.0

Table 6 Comparison of perforation velocities

No.	Impact velocity (m/s)	Perforation (m/s)		Error (%)
		Experimental	Computational	
1-2	1437	1333	1362	2.1
1-3	1333	1143	1281	2.0
1-4	1143	430*	1005	133.7
2-2	1450	1281	1380	7.7
2-3	1281	1014	1225	20.8
4-1	1461	1275	1380	8.2
4-2	1450	1325	1266	4.4
4-3	1325	1145	470	59.0

*Severe projectile erosion occurred

from other investigations. Any mismatch between the experimental and the calculated results must arise partly from the shortcomings of defining material properties. Nevertheless, as the following narrative demonstrates, acceptable results were obtained.

Definition of scabbing and disintegration of the concrete at points of entry and exit are a challenge, both computationally and physically. It is encouraging that the analytical capability represented by the software we have used provides a consistent basis for simulating the complex interaction between the missile and the concrete-steel bar matrix that it penetrates. The limitation we have faced is that we did not enjoy the privilege of selecting the ammunition, so only one type of anti-tank bullet was used in the tests.

Investigating the results listed in Tables 4-6, it can be seen that errors for various measures remain below 50 percent, especially for the crater at the rear face. These ratios were as small as 1.8 percent. Both experiments and the simulations demonstrate that scabbing and disintegration are directly related to the limiting tensile strain of concrete. This value increased steadily from Group 1 to Group 4, and the crater size on the entry and exit sides decreased steadily as a result.

The close agreement between calculated and measured entry-exit velocities suggests that the assumption that the bullet did not erode during its travel through the specimen is correct. The data in Table 6 enables the tentative conclusion also that higher concrete strength reduces missile velocity by a larger margin. It is stressed that the missed opportunity for measuring velocities in those specimens where no time window of filmed sequence showed the missile does not allow a more emphatic confirmation of this general trend. The only exception for this is for Specimen 1-4, the third in a series of targets resisting the same missile, where the missile did fracture to about one-third of its muzzle size. If this particular specimen is excluded, then remarkable accuracy is observed for exit velocities. This is a promising observation for extrapolating the analytical results to other types of weapons and target thicknesses for more rational protective structure design. While fiber reinforcement or its joint use with SIFCON tend to increase toughness, they do not provide improved resistance against missile penetration. Higher concrete strength appears to lead to excessive fracture, so this feature may represent reduced safety for enclosed personnel.

4. Investigation of the effect of steel bars and impact angle to the reduction of projectile velocity

Two related effects played a defining role on the measurements. One was the contact between the missile and reinforcement during its travel through the thickness of the specimen. The other was the slight bending of the missile trajectory as it penetrated successive specimens in its path, possibly as a consequence of prior metal-to-metal contact. It is proper to examine both of these effects.

Post-experiments inspection showed that the projectile had invariably struck directly or off-centrically the steel bars because of their dense configuration. Indeed, the state of the reinforcing cage in many of the pictures in Figs. 5-13 confirms bullet-bar contact. These steel bars seemed to increase the apparent tensile strength of the concrete and harness the lateral deformation. Empirical evidence showed that only the poorly consolidated or segregated parts of the concrete at the top of the form tended to spread laterally while the cage in the interior enforced integrity of the assembly. They also provided greater reduction in perforation velocity caused by the impact of the bullet on the bars.

Examination of the high-speed camera recordings showed that the projectiles had initially struck the specimens at what appeared to be a perfectly normal angle. However, inspection of missile holes in the slab suggested that slight path deviation might have taken place, especially when visual evidence existed that the bullet had struck a bar in its path. In the calculations, summarized in Fig. 14 for the 0.6 m thick specimens 1-2, 1-3 and 1-4, two sets of initial conditions were taken into consideration. First, initial contact was taken into account either as normal impact or at an impact angle of 2 degrees but the bullet did not impinge on any bar in its path. The curves “Normal” and “2 degrees” show the results of these runs. Next, contact of projectile on one of the longitudinal bars after first hit was considered in the simulations. Again, this occurs either after normal strike or a strike at 2 degree deviation from normal. The curves are collected in Fig. 14. The horizontal axis displays increments of 2 m, the spacing distance between slabs erected along the bullet’s path.

The missile velocity is reduced at an uneven rate in each case. An oblique impact results in faster decrease of velocity, with a slower velocity at entry resulting in greater rate of loss of velocity. Contact with the reinforcing steel bar worsens the velocity loss. Fig. 14(c) shows that an oblique hit

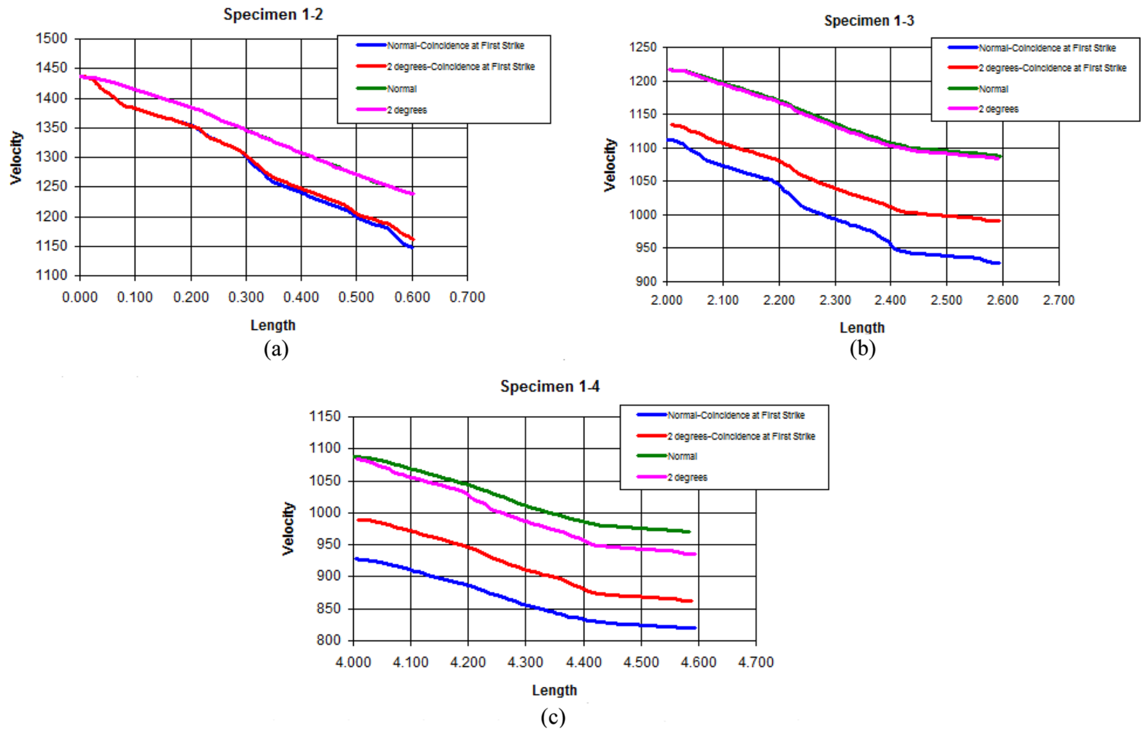

Fig. 14 Reduction of impact velocity (a) Specimen 1-2, (b) Specimen 1-3, (c) Specimen 1-4

at 2 degrees results in the smallest residual velocity after the bullet has penetrated three successive specimens in its path. We refrain from generalizing these findings as they represent a set of specialized initial conditions that may limit their global applicability.

5. Conclusions

In this paper, 8 of the experiments presented in Part I of this study (Korucu and Gülkan 2011) has been numerically simulated and validated by an extensive series of numerical computations. The primary objective of the study has been to measure the impact resistance to high-velocity impact of a large caliber projectile of traditionally manufactured, densely reinforced concrete targets made from ordinary Portland and calcium aluminate cement based HPSFRC and SIFCON concrete that had different compressive strengths and cement types. The ammunition that was used had a muzzle velocity of over 4 Mach. The targets were 2×2 m slabs with 0.6 m thickness including both reinforcement and steel fibers and only steel fibers. The shots resulted in complete perforation of the concrete even when targets were arranged such that three of them stood in series, with 2 m separating them. Impact and post-perforation velocities were measured by high-speed cameras. The measurements for some of the specimens could not be recorded due to human errors and poor weather conditions. Perforation, scabbing, shape of missile path and crater sizes were carefully measured on all specimens.

As a closing acknowledgment we must note that, the ordnance missile and the target we designed were not compatible with one another. The projectile has been designed to destroy armored tanks and similar tools of warfare whereas the target was designed to represent a part of a reinforced concrete protective structure. We used the weapon because it was the only type that was made available to us. It was helpful in ascertaining whether analytical capability existed for simulating the tests. We believe it did.

Concrete targets with a higher compressive strength showed a slightly better performance in reducing the initial impact velocity. A higher compressive strength enhances resistance against dynamic punching, although it also increases brittleness and the crater diameter in the event of failure. Steel fibers controlled the response and decreased crater dimensions and amount of spalling and scabbing. They did not show the expected performance in reducing the projectile velocity. By themselves, HPSFRC and SIFCON are not well-suited materials to resist supersonic projectiles such as used in the experiments even when both dense reinforcement and steel fibers have been used.

Unfortunately no records of the high-speed camera could be taken for the shots on Specimens 3-1, 3-2 and 3-3, that had been built using CAC-40 concrete. It was observed that the crater areas of these were smaller than specimens built using CEM I 42.5 R. The main reason for this difference is the higher compressive strength (87 MPa) for Group 3. In the absence of velocity measurements, however, no discerning comment can be made about the impact behavior of CAC-40 specimens by evaluating only crater sizes. We may advance the assumption that entry and exist velocities of the projectile cannot have been too different for these specimens from those recorded for Specimens 2-2 and 2-3, so an overall agreement of damage in the slab must be considered as predictive success.

ABAQUS/Explicit, our computational platform, gave acceptable results for the estimation of crater dimensions and residual velocities. We used a damaged plasticity model for concrete. The computational results did not match exactly the measurements on the specimens because our material parameters were defined only in terms of typical uniaxial stress-strain curves. The most important input for better-matched results would have been to use material models reflecting the actual physical conditions. To do so, material tests to determine the temperature dependent mechanical properties such as compressive and tensile strength, limiting strains, frictional interaction between concrete and tungsten must be carried out. Such tests could not be executed in the program. We have not found data in the literature that would enable an insight either. Nevertheless, the agreement between experimental and numerical results on the basis of elementary material characteristics cannot be overlooked.

The research reported herein achieved good agreement between theory and experiment after computational parameters were idealized for best match. A coupled problem such as a very high-velocity heavy caliber bullet impacting a flat concrete surface and penetrating it while it itself even slightly degrades in mass because of temperature and fragmentation poses a severe computational challenge. This has been satisfactorily, though not accurately, met in this investigation. Conventionally reinforced, high-strength concrete protective structures appear to be better than fiber reinforcement or SIFCON applications. Concrete toughness improves performance against scabbing and disintegration, an observation that is clearly observed in a comparative examination of the post-strike states of specimens in Groups 1, 2 and 4 (Figs. 6-13)

The results from this exploratory study are encouraging because it has been possible to simulate tests in the firing range in the computational domain. The missile designed to destroy armored targets was fired at thick reinforced concrete slabs instead. The action of the weapon on the target could be replicated with acceptable accuracy.

From the results obtained from experimental studies and numerical analyses, the following conclusions can be encapsulated:

– Thicker specimens have displayed a better performance in resisting the impact effects of the high-velocity projectile and reducing the perforation velocity. For protective facility design the principle of defense in thickness is valid. The amount of mesh reinforcement did not seem to cause much difference for the weapon used in the tests. The effect of reinforcement is observed in providing global integrity to the concrete and impeding its spalling and lateral disintegration upon receiving a direct hit.

– With mechanical and physical characteristics held constant, a higher concrete compressive strength enables a slightly improved performance in reducing the perforation velocity. This conclusion holds true for the type of concrete used in this phase of our study and may vary for other types of aggregates. Concrete ductility, expressed as ultimate strain limits, improves reduction of degradation of the concrete matrix (Figs. 6-13).

– Reinforced concrete is no match in resisting supersonic projectiles such as those used in the experiments even when dense reinforcement has been provided. It is unlikely that this type of ammunition would be used against a reinforced concrete target in a hostile environment, except accidentally, so more directly useful results would be derived from tests on more plausible combinations of target and weapon.

– ABAQUS/Explicit yielded satisfactory results for the estimation of residual velocity. Its predictive capability for crater sizes is adequate for engineering applications. Numerical results for estimating crater dimensions did not match accurately the dimensions measured on the specimens. The main reason for this deviation is believed to be the inadequate description of material parameters at extreme strain rates and heat interaction. The most important requirement for well-matched results would be to use material models reflecting the actual material under the set of circumstances described. To do so, detailed material tests must be carried out such that temperature dependent compressive, tensile and shear strength can be established.

– Assumption of non-eroding missile models in computations would yield results that are conservative.

– Oblique bullet strike on a flat surface and its collision with reinforcement during its course through the concrete matrix tend to enhance velocity reduction.

Acknowledgments

This work was funded by TUBITAK (The Scientific and Technological Research Council of Turkey) under project No.106M497. The firing range, shot projectiles and help personnel were made available by the Turkish Armed Forces. We acknowledge both sources for their generous support during the conduct of the research. Our thanks are extended to the many officers and enlisted men who worked, often under very adverse climatic conditions in the remotely located firing range, to assist us setting up our experimental arrangements while meeting their regular obligations.

References

Bhargava, P., Sharma, U.K. and Kaushik, S.K. (2006), "Compressive stress-strain behavior of small scale steel fiber reinforced high strength concrete cylinders", *J. Adv. Concrete Tech.*, **4**(1), 109-121.

Dassault Systemes (2007), ABAQUS Theory Manual, Version 6.7, Simulia, Providence, Rhode Island.
Eleiche, A.S.M. (1972), A literature survey of the combined effects of strain rate and elevated temperature on the mechanical properties of metals, Air Force Materials Laboratories, Report AFML-TR-72-125.
Hong, T., Ooi, J.Y. and Shaw, B.A. (2008), "A three-dimensional finite element analysis of two/multiple shots impacting on a metallic component", *Struct. Eng. Mech.*, **29**(6), 709-729.
Huang, F., Wu, H., Jin, Q. and Zhang, Q. (2005), "A numerical simulation on the perforation of reinforced concrete targets", *Int. J. Impact Eng.*, **32**, 173-187.
Korucu, H. and Gülkan, P. (2011), "High-velocity impact of large caliber tungsten projectiles on ordinary Portland and calcium aluminate cement based HPSFRC and SIFCON slabs. Part I: Experimental investigations", *Struct. Eng. Mech.*, **40**(5), 595-616.
Kumar, S. (2010), "Analysis of impact response and damage in laminated composite cylindrical shells undergoing large deformations", *Struct. Eng. Mech.*, **35**(3), 349-364.
Lee, J. and Fenves, G.L. (1998), "Plastic-damage model for cyclic loading of concrete structures", *J. Eng. Mech. ASCE*, **124**(8), 892-900.
Li, F. and Li, Z. (2001), "Continuum damage mechanics based modeling of fiber reinforced concrete in tension", *Int. J. Solids Struct.*, **38**(5), 777-793.
Lindholm, J.S. and Besseny, R.L. (1969), A Survey of Rate Dependent Strength Properties of Metals, Air Force Materials Laboratory, Report AFML-TR-69-119.
Lubliner, J., Oliver, J., Oller, S. and Oòate, E. (1989), "A plastic-damage model for concrete", *Int. J. Solids Struct.*, **25**(3), 229-326.
Naaman, AE. (1992), SIFCON: Tailored properties for structural performance, *High Performance Fiber Reinforced Cement Composites*, RILEM Proceedings 15, E & FN Spon, London.
Rousseau, J., Frangin, E., Marin, P. and Daudeville, L. (2008), "Damage prediction in the vicinity of an impact on a concrete structure: a combined FEM/DEM approach", *Comput Concrete*, **5**(4), 343-358.
Shiu, W., Donze, F.V. and Daudeville, L. (2008), "Compaction process in concrete during missile impact: a DEM analysis", *Comput Concrete*, **5**(4), 329-342.
Siddiqui, N.A., Khan, F.H. and Umar, A. (2009), "Reliability of underground concrete barriers against normal missile impact", *Comput Concrete*, **6**(1), 79-93.
Symonds, P.S. (1967). Survey of Methods of Analysis for Plastic Deformation of Structures under Dynamic Loading, Brown University, Division of Engineering, Report BU NSRDC 167.

Appendix A: Notation

Symbols have the following definitions:

d	scalar stiffness degradation variable
D^{el}	degraded elastic stiffness
D_0^{el}	degraded initial (undamaged) elastic stiffness
E_0	initial (undamaged) elastic stiffness of the material
E_s	Young's modulus for steel
E_t	Young's modulus for tungsten
$\dot{\varepsilon}$	total strain rate
$\dot{\varepsilon}^{el}$	elastic part of the strain rate
$\dot{\varepsilon}^{pl}$	plastic part of the strain rate
$\dot{\bar{\varepsilon}}^{pl}$	equivalent plastic strain rate
σ	the cauchy stress
σ_c^c	stress under uni-axial compression for concrete
σ_t^c	stress under uni-axial tension
σ_u^s	ultimate stress under uni-axial tension for steel
σ_y^s	yield stress under uni-axial tension for steel
$\bar{\sigma}$	yield stress at nonzero plastic strain rate
$\bar{\sigma}_c$	effective uni-axial cohesion stress in compression
$\bar{\sigma}_t$	effective uni-axial cohesion stress in tension
$\bar{\sigma}^{def}$	effective stress
ν_s	Poisson's ratio for steel
ν_t	Poisson's ratio for tungsten

Appendix B: Theory of damaged plasticity model for concrete

Strain rate decomposition is defined as

$$\dot{\varepsilon} = \dot{\varepsilon}^{el} + \dot{\varepsilon}^{pl} \tag{B.1}$$

where $\dot{\varepsilon}$ is the total strain rate, $\dot{\varepsilon}^{el}$ is the elastic part of the strain rate, and $\dot{\varepsilon}^{pl}$ is the plastic part of the strain rate.

The stress-strain relations are

$$\sigma = (1-d)D_0^{el}/(\varepsilon - \varepsilon^{pl}) = D^{el}/(\varepsilon - \varepsilon^{pl}) \tag{B.2}$$

where D_0^{el} is the degraded initial (undamaged) elastic stiffness of the material; $D^{el} = (1-d)D_0^{el}$ is the degraded elastic stiffness; and d is the scalar stiffness degradation variable, which can take values in the range from zero (undamaged material) to one (fully damaged material).

The effective stress is defined as

$$\bar{\sigma}^{def} = D_0^{el}/(\varepsilon - \varepsilon^{pl}) \tag{B.3}$$

The Cauchy stress has a relationship to the effective stress as

$$\sigma = (1-d)\bar{\sigma} \tag{B.4}$$

Tensile and compressive damaged states are described separately by two hardening variables, $\tilde{\varepsilon}_t^{pl}$ and $\tilde{\varepsilon}_c^{pl}$. The evolution of these variables is given by

$$\tilde{\varepsilon}^{pl} = \begin{bmatrix}\tilde{\varepsilon}_t^{pl}\\ \tilde{\varepsilon}_c^{pl}\end{bmatrix}; \qquad \dot{\tilde{\varepsilon}}^{pl} = h(\bar{\sigma}, \tilde{\varepsilon}^{pl}).\dot{\varepsilon}^{pl} \tag{B.5}$$

The yield function, $F(\bar{\sigma}, \tilde{\varepsilon}^{pl})$, describes a surface in effective stress space that determines the states of failure or damage. For the plastic-damage model

$$f(\bar{\sigma}, \tilde{\varepsilon}^{pl}) \le 0 \tag{B.6}$$

Plastic flow occurs according to the flow rule

$$\dot{\varepsilon}^{pl} = \dot{\lambda}\frac{\partial G(\bar{\sigma})}{\partial \bar{\sigma}} \tag{B.7}$$

where $\dot{\lambda}$ is the nonnegative plastic multiplier, and G is the flow potential.

Uniaxial stress-strain curves can be transformed into stress versus plastic strain curves of the form

$$\sigma_t = \sigma_t(\tilde{\varepsilon}_t^{pl}, \dot{\tilde{\varepsilon}}_t^{pl}, \theta, f_i) \tag{B.8}$$

$$\sigma_c = \sigma_c(\tilde{\varepsilon}_c^{pl}, \dot{\tilde{\varepsilon}}_c^{pl}, \theta, f_i) \tag{B.9}$$

where $\dot{\tilde{\varepsilon}}_t^{pl}$ and $\dot{\tilde{\varepsilon}}_c^{pl}$ are the equivalent plastic strain rates, $\tilde{\varepsilon}_t^{pl} = \int_0^t \dot{\tilde{\varepsilon}}_t^{pl} dt$ and $\tilde{\varepsilon}_c^{pl} = \int_0^t \dot{\tilde{\varepsilon}}_c^{pl} dt$ are the equivalent plastic strains, θ is the temperature, and f_i, $(i = 1,2,3,\cdots)$ are other predefined field variables.

The effective plastic strain rates are given as

$$\dot{\tilde{\varepsilon}}_t^{pl} = \dot{\varepsilon}_{11}^{pl}\text{, in uniaxial tension} \tag{B.10}$$

and

$$\dot{\tilde{\varepsilon}}_c^{pl} = -\dot{\varepsilon}_{11}^{pl}\text{, in uniaxial compression} \tag{B.11}$$

The degraded response of concrete is characterized by two independent uniaxial damage variables, d_t and d_c, which are assumed to be functions of the plastic strains, temperature, and field variables

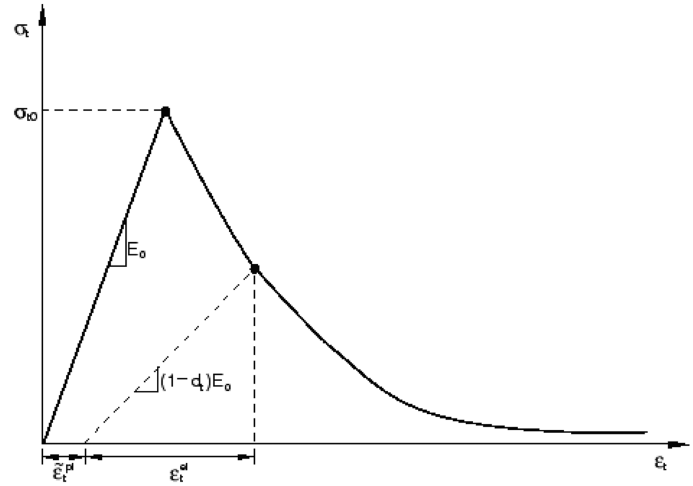

Fig. B1 Response of concrete to uniaxial loading in tension (Dassault Systemes 2007)

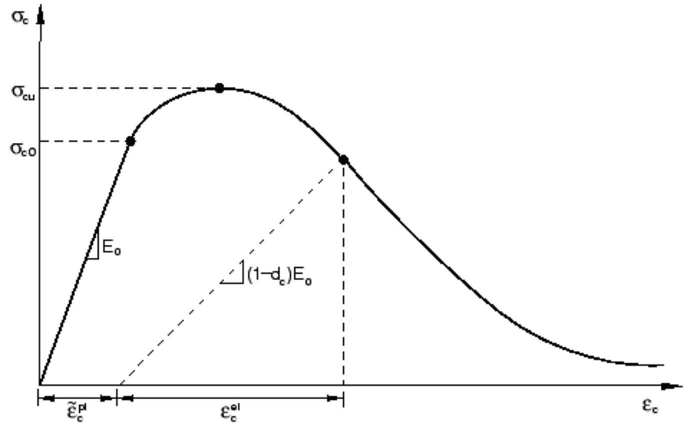

Fig. B2 Response of concrete to uniaxial loading in compression (Dassault Systemes 2007)

$$d_t = d_t(\tilde{\varepsilon}_t^{pl}, \theta, f_i), \quad (0 \le d_t \le 1) \tag{B.12}$$

$$d_c = d_c(\tilde{\varepsilon}_c^{pl}, \theta, f_i), \quad (0 \le d_c \le 1) \tag{B.13}$$

Figs. B1 and B2 show response of concrete to uniaxial loading in tension and compression, respectively.

The stress-strain relations under uniaxial tension and compression loading are, respectively

$$\sigma_t = (1-d_t)E_0(\varepsilon_t - \tilde{\varepsilon}_t^{pl}) \tag{B.14}$$

$$\sigma_c = (1-d_c)E_0(\varepsilon_c - \tilde{\varepsilon}_c^{pl}) \tag{B.15}$$

where E_0 is the initial (undamaged) elastic stiffness of the material.

The effective uni-axial cohesion stresses, $\bar{\sigma}_t$ and $\bar{\sigma}_c$ are

$$\bar{\sigma}_t = \frac{\sigma_t}{(1-d_t)} = E_0(\varepsilon_t - \tilde{\varepsilon}_t^{pl}) \tag{B.16}$$

$$\bar{\sigma}_c = \frac{\sigma_c}{(1-d_c)} = E_0(\varepsilon_c - \tilde{\varepsilon}_c^{pl}) \tag{B.17}$$

Appendix C: Theory of rate-independent plasticity model for steel

Rate-independent plasticity is used in modeling the response of steel bars. Rate dependence can be introduced using an overstress power law

$$\dot{\bar{\varepsilon}}^{pl} = D\left(\frac{\sigma}{\sigma_o} - 1\right)^n \quad \text{for } \bar{\sigma} \ge \sigma^0 \tag{C.1}$$

where $\dot{\bar{\varepsilon}}^{pl}$ is the equivalent plastic strain rate; $\bar{\sigma}$ is the yield stress at nonzero plastic strain rate; $\sigma^0(\varepsilon^{pl}, \theta, f_i)$ is the static yield stress and $D(\theta, f_i)$, $n(\theta, f_i)$ are material parameters (Symonds 1967, Lindholm *et al.* 1969, Eleiche 1972).